Volume 11 | Number 12 | 28 March 2019 | Pages 5119–5774

Nanoscale

rsc.li/nanoscale

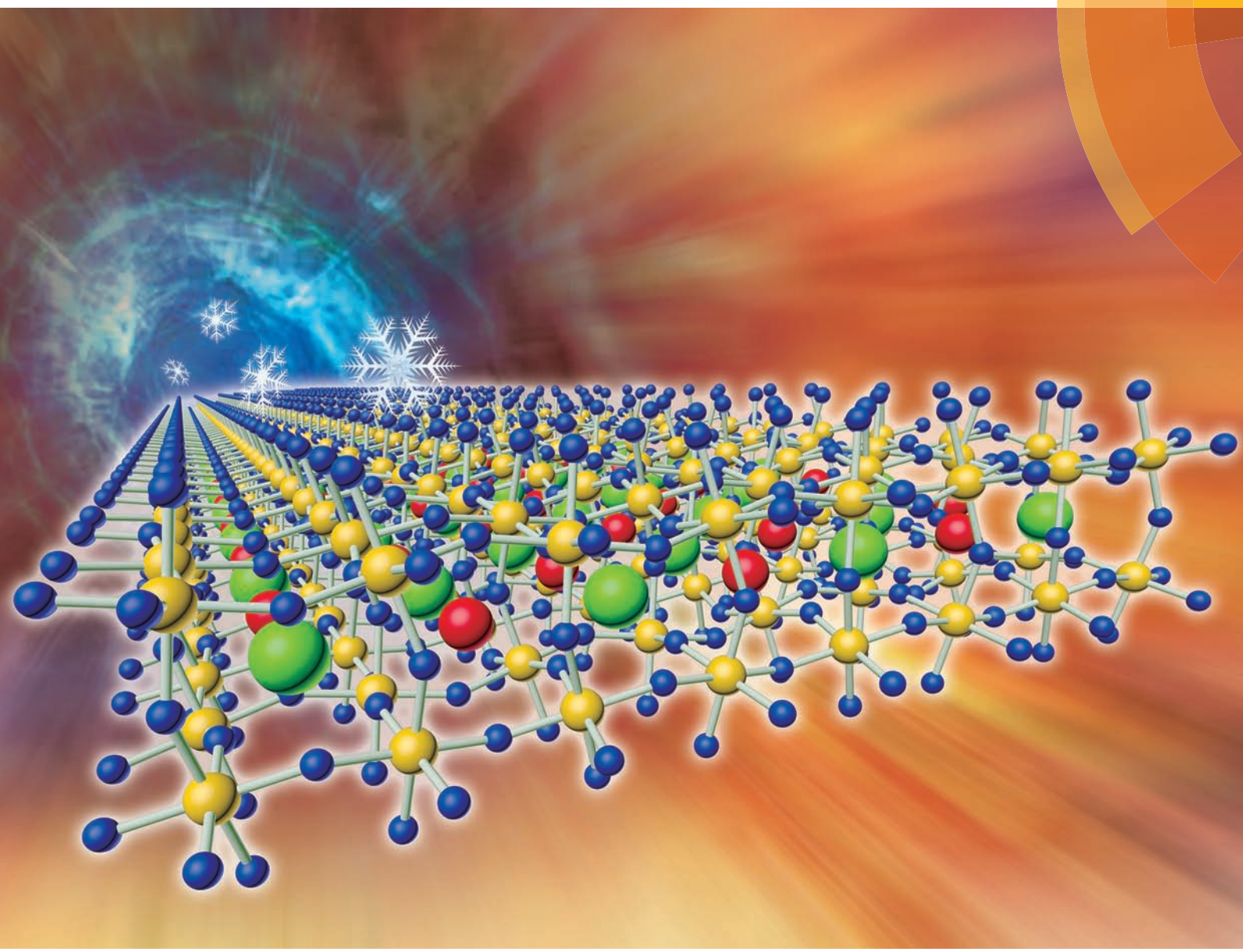

ISSN 2040-3372

ROYAL SOCIETY OF CHEMISTRY | Celebrating IYPT 2019

PAPER
Zhubing He, Rui Chen *et al.*
Influence of mixed organic cations on the structural and optical properties of lead tri-iodide perovskites

NCNST

Nanoscale

PAPER

View Article Online
View Journal | View Issue

Check for updates

Cite this: *Nanoscale*, 2019, **11**, 5215

Influence of mixed organic cations on the structural and optical properties of lead tri-iodide perovskites†

Guotao Pang,[a,c] Xiaoqi Lan,[b,c] Ruxue Li,[a] Zhubing He *[b] and Rui Chen *[a]

Received 4th December 2018,
Accepted 28th December 2018

DOI: 10.1039/c8nr09795j

rsc.li/nanoscale

Perovskites with mixed organic cations possess better properties in some aspects as compared to their pure counterparts. However, the structural and optical properties of these mixed-type perovskites have been rarely investigated. In this study, probable structures of mixed organic cation perovskites, $MA_xFA_{1-x}PbI_3$ (x = 1, 0.8, 0.6, 0.4 and 0.2), were comparatively discussed. Saturation of excitonic emission at 1.66 eV indicates limited orthorhombic phase at 30 K in $MAPbI_3$, which confirms the co-existence of orthorhombic and tetragonal phases at low temperatures. Based on the comprehensive temperature- and power-dependent measurements, it is found that defects are activated in mixed organic cation perovskites under low excitation power at room temperature, whereas this process is not observed in pure $MAPbI_3$. At high excitation power, free exciton recombination is suppressed due to exciton–exciton interaction for all samples. Analysis of stability against temperature based on these photoemission processes shows that the structure with comparable organic cation proportion is more stable; this can be explained by uniformly distributed strains existing at the boundaries between $MAPbI_3$ and $FAPbI_3$ molecules. These analyses of structural and optical properties of mixed organic cation perovskites are meaningful in dictating the future optoelectronic devices.

1. Introduction

Perovskite materials have been widely investigated because of their novel properties such as large light absorption coefficient,[1–3] long carrier diffusion length,[4,5] and tunable bandgap.[6] The power conversion efficiency of perovskite-based solar cells has exceeded 23%;[7–9] thus, these materials are developing much faster as compared to conventional materials. Recently, the external quantum efficiency of perovskite light-emitting diodes has reached 20%.[10,11] Moreover, wide exploration of optical-pumped lasing in solution-processed perovskite structures shows great preponderance for optoelectronic applications.[12,13] Although significant potential has been shown in all the abovementioned fields, the quest for higher performance perovskite-based devices demands deep insights into their structural and optoelectronic properties. Compared to inorganic perovskites, hybrid organic–inorganic perovskite materials show better performance.[4,14,15] However, the stability of the related devices is still a problem that needs to be resolved.[16,17] It has been theoretically and experimentally reported that the mixed-cation or -anion perovskite materials are more stable as compared to their pure counterparts.[18–20] Moreover, mixed organic cation optoelectronic devices showing superior performance have been demonstrated.[21] However, only few studies have been conducted to clarify the related optical properties. Therefore, it is essential to investigate the physical mechanism of the stability and optical properties of the mixed-type perovskites.

In this study, the structural and optical properties of $MA_xFA_{1-x}PbI_3$ (MA: $CH_3NH_3^+$ and FA: $CH(NH_2)_2^+$) have been investigated, and the underlying physical mechanism for the improved thermal stability has been discussed. Temperature-dependent measurements have been carried out to analyze the structural phase transition, which would be meaningful for the future application of perovskite-based optoelectronic devices.

[a]*Department of Electrical and Electronic Engineering, Southern University of Science and Technology, Shenzhen 518055, P. R. China. E-mail: chen.r@sustc.edu.cn*
[b]*Department of Materials Science and Engineering, Shenzhen Key Laboratory of Full Spectral Solar Electricity Generation (FSSEG), Southern University of Science and Technology, Shenzhen 518055, P. R. China. E-mail: hezb@sustc.edu.cn*
[c]*Harbin Institute of Technology, Harbin 150001, P. R. China*
†Electronic supplementary information (ESI) available. See DOI: 10.1039/c8nr09795j

2. Experimental

2.1 Materials

High-purity (99.99%) PbI_2 was purchased from Alfa Chemical Group. MAI and FAI with a purity of more than 99.5% were

purchased from Luminescence Technology Corp. (LUMTEC). To prepare $MA_xFA_{1-x}PbI_3$ (x = 1, 0.8, 0.6, 0.4 and 0.2) solutions with a concentration of 1 mol L^{-1}, MAI and FAI powders with the corresponding molar ratios, together with PbI_2, were added to DMF and DMSO, which had a volume ratio of 7 : 3. Quantity of all these regents could be easily calculated. After this, all five solutions were stirred at the rate of 300 rpm and heated at 60 °C for 2 hours. Prior to spin coating on quartz substrates, the solution was filtered with 0.22 μm polytetrafluoroethylene (PTFE) filters. Finally, thin films of about 250 nm, estimated by transmission electron microscopy (TEM) through the intramolecular exchange method, were prepared.[15,22] To avoid the degradation of samples, another quartz substrate was used to capsulate the thin film. Pure $FAPbI_3$ has not been synthesized successfully using this method because black α-$FAPbI_3$ is not stable and easily collapses into yellow β-$FAPbI_3$ structures at room temperature.[19,20] However, the stable structure can be obtained when the proportion of FA is more than 20%.[21] Films fabricated by the abovementioned method are dense and uniform.[22] Therefore, the structural and optical analyses of these samples will be meaningful.

2.2 Structural properties

Fig. 1a presents the X-ray diffraction (XRD) spectra of $MA_xFA_{1-x}PbI_3$ (x = 1, 0.8 0.6 0.4 and 0.2), which confirm the cubic phase of the perovskite materials. All crystal planes correspond well with the previous reports.[23] To discuss the influence of the organic cations, (100) plane is selected for comparison. It is found that the peak positions of the XRD spectra show a slight shift towards a lower angle with an increase in the FA proportion. As is known, the crystal lattice size of $FAPbI_3$ is larger than that of $MAPbI_3$; thus, according to the Bragg equation, a higher content of FA cation in $MA_xFA_{1-x}PbI_3$ will lead to a shift of the XRD peaks towards lower angle;[24] this is consistent with the observation shown in Fig. 1b. Moreover, the full width at half maximum (FWHM) becomes wider as the proportion of FA increases until x = 0.6, and then, it becomes narrower when the proportion of FA increases further; this indicates slight differences in the crystal domain size of five samples. According to the Scherrer equation, the purer the organic cations, the larger the crystal domain. Other crystal planes display similar trends as the (100) plane and are shown in Fig. S1.† By comparing the characteristics of the XRD data of these samples, we can conclude that the FA and MA molecules are distributed uniformly inside the materials. The molecular sizes of MA and FA are different; therefore, strain will be induced at the boundaries between them and uniformly distributed inside the crystals. The uniformly distributed strains count for the final pure cubic phase although the organic cations are changing. Fig. 1c shows the possible schematic structures of $MA_xFA_{1-x}PbI_3$ (x = 0.2 and 0.6), which are drawn based on the XRD spectra and the abovementioned synthetic method. Note that the Pb–I–Pb bond is not 180° at room temperature.[25] Angles of this kinds of bonds are determined by the size of the organic cations. The bond angle will be close to 180° if the organic cation is bigger. As shown in Fig. 1c, $MA_{0.2}FA_{0.8}PbI_3$ shows a larger crystal lattice size than $MA_{0.6}FA_{0.4}PbI_3$. This is because of the larger size of FA as compared to that of MA;[24] this results in the larger Pb–I–Pb bond angle in the crystal.

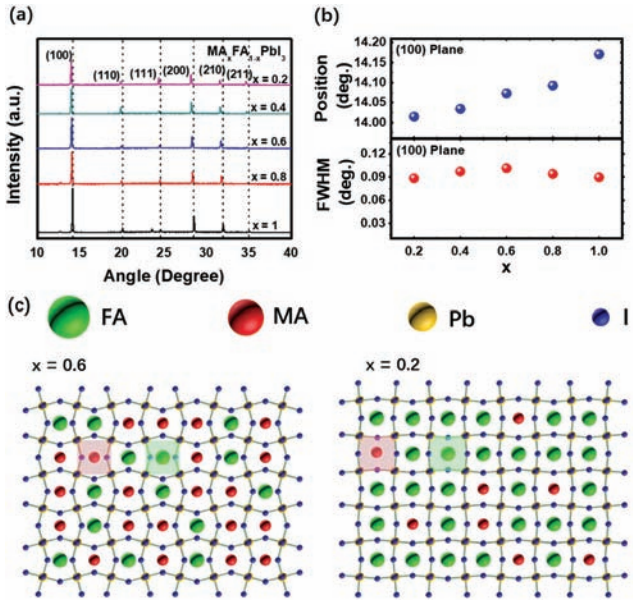

Fig. 1 (a) XRD spectra of $MA_xFA_{1-x}PbI_3$ (x = 1, 0.8, 0.6, 0.4, and 0.2) at room temperature, (b) peak position and FWHM of (100) XRD peak of $MA_xFA_{1-x}PbI_3$, (c) structures of $MA_xFA_{1-x}PbI_3$ (x = 0.2 and 0.6). Shallow green squares in the figure refer to the relative size of cubic phases of two samples at room temperature.

3. Results and discussion

3.1 Photoluminescence spectra of $MA_xFA_{1-x}PbI_3$

To investigate the influence of structures on the optical properties, absorption and photoluminescence (PL) measurements were conducted at room temperature, as shown in Fig. 2a and b, for MA = 0.6 and MA = 1, respectively. Spectra of other samples can be found in Fig. S2.† The excitation source for measurements is a diode laser operating at 660 nm with a power of 10 mW. To determine the bandgap of different samples, linear regions of absorbance spectra are extracted and fitted. Stokes shifts are very small for all samples; this indicates the recombination of free excitons,[26] which has been discussed later. Fig. 2c shows the bandgap fitting using the Vegard's Law. Herein, the bandgap of pure $FAPbI_3$ at room temperature is obtained from a previously reported study.[2] For the mixed organic cation perovskites, bandgaps increase linearly with an increase in the MA proportion. Herein, pure $MAPbI_3$ and $FAPbI_3$ significantly deviate from the fitting curve; this may be due to the peculiar rotational properties of MA and FA cations, as reported in ref. 18. To determine the influence of structures on the optical properties, PL measurements of the samples were conducted at room (295 K) and low (30 K)

 This journal is © The Royal Society of Chemistry 2019

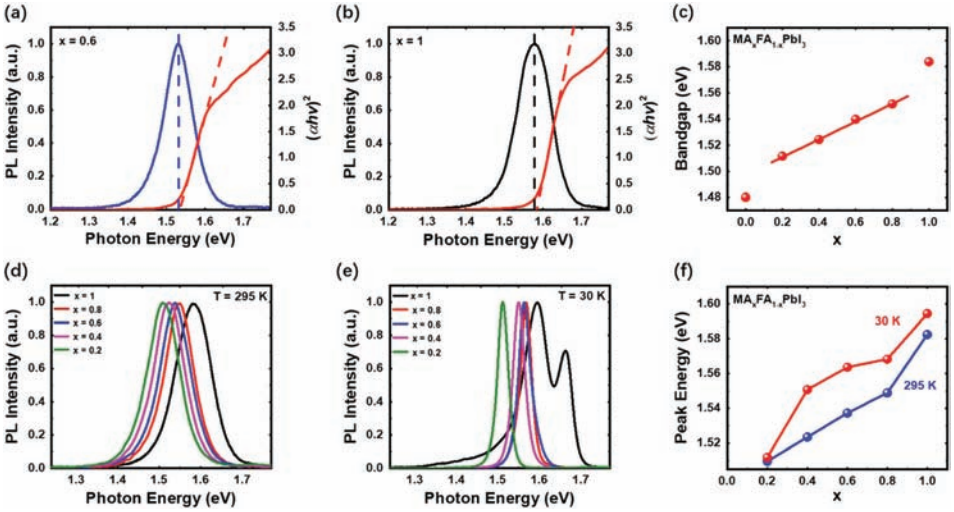

Fig. 2 (a) and (b) Steady-state absorption and photoluminescence of $MA_xFA_{1-x}PbI_3$ (x = 0.6 and 1). (c) Bandgaps of $MA_xFA_{1-x}PbI_3$ (x = 1, 0.8, 0.6, 0.4, and 0.2) indicated from absorption at room temperature. (d) and (e) PL spectra at 295 K and 30 K, respectively. (f) Peak positions of the corresponding PL spectra at 295 K and 30 K, respectively.

temperatures, as shown in Fig. 2d and e, respectively. PL peak energies decrease as the proportion of FA increases at various temperatures; this is consistent with bandgap variations as shown in Fig. 2c. Therefore, the PL emission can be attributed to the near-bandgap recombination. In the absorbance spectra at room temperature, there is no obvious excitonic peak. In this case, the exciton screen effect induced by the collective orientational motion of the organic cations at room temperature counts.[27] Note that the FWHM of PL spectra at 295 K is obviously wider than that at 30 K; this is due to the exciton–phonon interaction. For pure $MAPbI_3$, multi-peak emission appears at 30 K, whereas for the mixed organic cation perovskites, single emission peak appears at the same temperature. In Fig. 2f, the peak positions of five samples at various temperatures are plotted. For mixed organic cation perovskite materials, the PL peak positions at 295 K shift linearly as the proportion of MA increases. In addition, this trend corresponds well with that of the bandgaps shown in Fig. 2c. However, the PL peak positions at 30 K are significantly different from those at room temperature as the corresponding peak energies increase nonlinearly and reach saturation as the proportion of MA increases. The deviation from linear relationship indicates great difference of exciton binding energy as the organic cation proportion changes. The pure $MAPbI_3$ is slightly different; this may due to the rotational properties of MA cation, as mentioned above.

To further investigate the recombination mechanisms at 30 K, PL spectra of $MAPbI_3$ were obtained. As abovementioned, pure $MAPbI_3$ demonstrates multi-peak emission. It can be observed from Fig. 3a that there are three emission peaks that can be well-fitted by Gaussian functions. This fine structure may result from the mixed orthorhombic-tetragonal structural phases, as reported previously.[28,29] Power-dependent PL measurements have been carried out to clarify the origin of

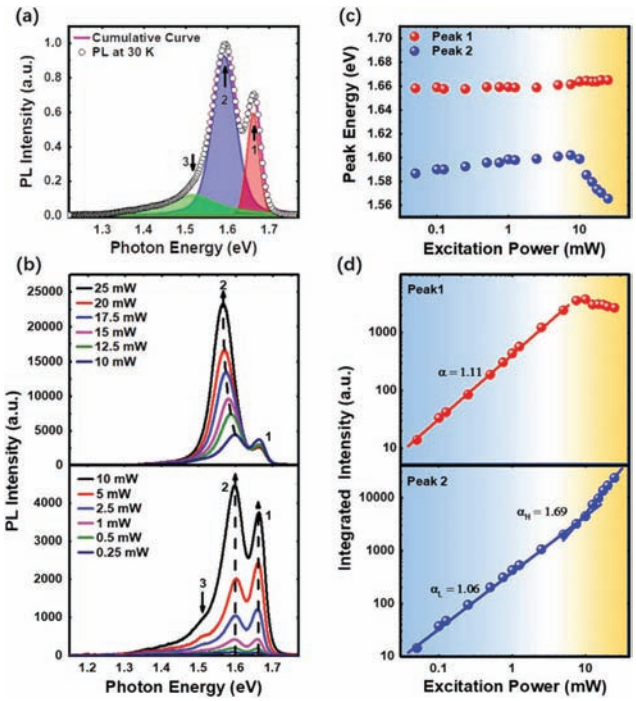

Fig. 3 (a) Excitonic peaks of $MAPbI_3$ at 30 K, (b) power-dependent PL spectra of $MAPbI_3$, (c) power-dependent peak energy of $MAPbI_3$ at 30 K, and (d) integrated intensity of two main excitonic peaks at 30 K.

these emissions. As shown in Fig. 3b, three peaks under low power excitation can be clearly observed. Peak 3, which is located at the lowest energy side, is noticeable. However, as the laser power increases to a value as high as 25 mW, peak 3 becomes far from being comparable with another two peaks. Peak 1 displays novel behaviour as there is saturation when the

power is higher than 7.5 mW. Moreover, peak 2 increases faster as compared to the low power situation. The saturation of high energy peak is due to the limited amount of orthorhombic phase in the crystal. There is a big energy difference between peak 2 and peak 1, which is much larger than the energy of the longitudinal optical (LO) phonons.[28] Thus, peak 2 could result from the free exciton recombination of lower energy tetragonal phase. In addition, the lowest energy side peak 3 originated from the bound exciton recombination of the tetragonal phase, as has been reported previously.[30] The mixed-phase structure means that the $MAPbI_3$ sample is exactly located in the phase transition range at this temperature. This result contradicts with some reports, in which the phase transition appears at higher temperatures.[30–32] Fig. 3c shows the photon energy of peak 1 and peak 2. As the power increases from 0.05 to 7.5 mW, both peaks demonstrate a blue shift, and it is more obvious for peak 2. However, when the power increases continuously from 7.5 mW, peak 2 experiences a dramatic red shift. The photo-induced electrons transfer from the saturated orthorhombic phase to the tetragonal phase and contribute to the tetragonal phase-related emission. Huge amount of heat is released in this process and results in the abrupt red shift of peak 2, which is related to the instability of the tetragonal phase under high power excitation in the phase transition range. It is shown that the crystal structure in the phase transition range has a significant influence on the optical properties of perovskite materials. Fig. 3d shows the integrated intensity of two peaks varying in a wide power range. The data are fitted by eqn (1), which can be derived from the recombination equations.[26]

$$I = I_0^{\alpha} \tag{1}$$

where I refers to the integrated PL intensity and I_0 is the excitation power. α herein indicates the emission mechanisms. It is expected to be close to 1 for monomolecular recombination and around 2 for bimolecular recombination. For peak 1, the exponential index α is around 1.11 under low excitation power, which indicates the free exciton recombination in the orthorhombic phase. Peak 2 shows a similar recombination mechanism in this power range, where α_L (α under low excitation power) is 1.06. As the power increases continuously, peak 1 displays saturation, and at the same time, peak 2 increases significantly with the index α_H (α under high excitation power) of this process being 1.69, which is higher than that at lower power. Obviously, there is energy transfer from the saturated orthorhombic phase to the tetragonal phase; this increases the probability of the formation of free excitons in this region. Therefore, two regimes for the formation of free excitons in the tetragonal phase could be seen at the same time: one is from the laser excitation directly, and another is from the carrier transfer inside the crystal.

To further confirm the co-existence of two phases, the temperature-dependent PL measurements have been performed under a laser power of 10 mW, where peak 1 begins to saturate, as shown in Fig. 4a. The contour plot of PL emission

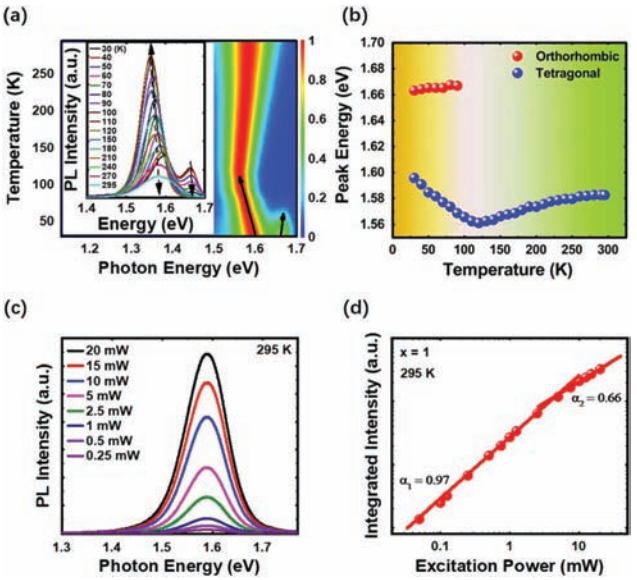

Fig. 4 (a) Normalized temperature-dependent two-dimensional contour PL image of $MAPbI_3$ from 30 K to 295 K (inset shows the PL spectra from 30 K to 110 K), (b) peak energy of $MAPbI_3$ from 30 K to 295 K, (c) power-dependent PL spectra and (d) integrated peak intensity of $MAPbI_3$ at 295 K.

from 30 to 295 K is given in Fig. 4a, and the inset shows the PL spectra. At 30 K, both the orthorhombic phase (high-energy side) and tetragonal phase (low-energy side) co-exist. Black solid arrows indicate the change in the peak position of two phases from 30 to 110 K. As temperature increases, peak 2 shows a significant red shift, whereas peak 1 experiences a slight blue shift (as shown in Fig. 4b). This is consistent with the power-dependent measurement at 30 K and further confirms the existence of a thermal effect. Moreover, peak 1 displays thermal quenching as the temperature increases, whereas the intensity of peak 2 experiences an enhancement. At around 110 K, peak 1 disappears and peak 2 reaches its maximum. This is exactly the end of the phase transition range, and above this temperature, peak 2 starts to quench and demonstrate a blue shift, indicated by black dashed arrows in the inset of Fig. 4a. The analysis further confirms the co-existence of the orthorhombic and tetragonal phases at low temperatures. At around 110 K, all the orthorhombic phase structures develop into tetragonal phase structures, and the emission starts to shift to the short-wavelength side. In the mixed-phase crystal structure, it is noted that the orthorhombic phase is the stable phase, whereas the tetragonal phase is not. This can be explained by the red shift of peak 2 and blue shift of peak 1 as the temperature increases from 30 to 110 K; this is in agreement with the analysis results shown in Fig. 3. Fig. 4c shows the power-dependent spectra of $MAPbI_3$ at room temperature, and Fig. 4d shows the corresponding PL integrated intensity. Under low-power excitation, the integrated PL intensity increases with the exponential index α_1 = 0.97. Herein, recombination of free excitons plays a dominant role. However, as the power increases continuously,

 This journal is © The Royal Society of Chemistry 2019

the exponential index α_2 declines to 0.66, which is much smaller than 1. The dramatic change in α may be due to the exciton–exciton interaction under high-power excitation,[33] during which the probability of radiative recombination declines in an Auger-like process.

To clarify the influence of organic cations on the optical properties, mixed organic cation perovskites were explored at 30 K and room temperature. Power-dependent PL spectra were obtained at both temperatures, and all samples displayed single emission characteristics. Actually, the optical properties of mixed cation perovskite are similar to those of pure $MAPbI_3$ at 30 K, except that there is no saturation or dramatic increase in the PL integrated peak intensity. It can be seen from Table 1 that all the exponential indices α of power-dependent measurements are very close to 1 for the whole power range; this means that there is only free exciton recombination at low temperatures. However, at room temperature, α_L for all samples are larger than 1. It is obviously larger than that of pure $MAPbI_3$ in which free exciton recombination plays a key role under low-power excitation. Photoexcited carriers in unintentional dopants or defects contribute to the formation of free excitons in this case,[26] which may be induced by the mixing of MA and FA. These dopant- or defect-trapped carriers are activated at higher temperatures. Under higher excitation power, exponential indices (α_H) become smaller than 1 for all the four samples. This is just because of the abovementioned exciton–exciton interaction in the analysis of $MAPbI_3$.

3.2 Stability of $MA_xFA_{1-x}PbI_3$ against temperature

The photoemission process provides good insight for the exploration of stability of mixed organic cation perovskites against changes in the temperature. A 2D contour plot of the normalized PL spectra of $MA_{0.8}FA_{0.2}PbI_3$ is shown in Fig. 5a. Perovskite semiconductor materials are very different from conventional semiconductors in terms of band gap shrinkage at high temperatures. A contrary blue shift for perovskite material is observed, which has been discussed above for pure $MAPbI_3$. According to the analysis for pure $MAPbI_3$ shown in Fig. 3 and 4, the PL peak will experience a blue shift when the phase transition is completed. The change in the peak position from red shift to blue shift can be denoted as the end of the phase transition range. Similarly, the start of the phase transition range is indicated by the change in the peak position from blue shift to red shift. As shown in Fig. 5a, the phase transition range for $MA_{0.8}FA_{0.2}PbI_3$ is marked by two dashed horizontal lines. There is a red shift in this temperature range, and as mentioned in the analysis of $MAPbI_3$, the structure in

Table 1 Power-dependent index of $MA_xFA_{1-x}PbI_3$ (x = 0.8, 0.6, 0.4, 0.2) at 30 and 295 K

T (K)	Index	x = 0.8	x = 0.6	x = 0.4	x = 0.2
30	α	1.02	1.00	1.04	1.03
295	α_L	1.55	1.27	1.73	1.31
	α_H	0.80	0.55	0.75	0.83

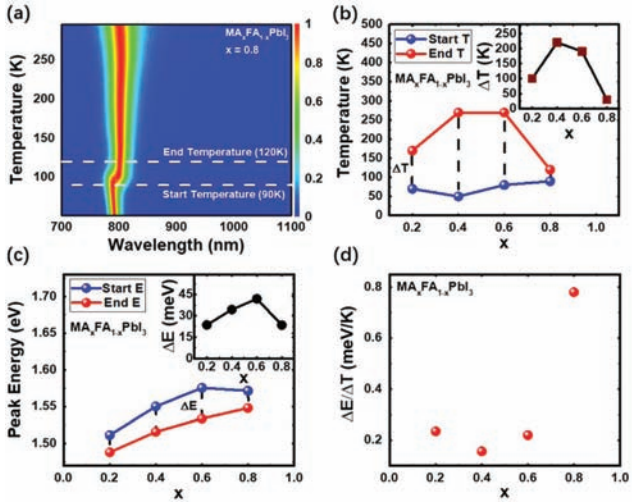

Fig. 5 (a) Temperature-dependent PL spectra of $MA_{0.8}FA_{0.2}PbI_3$, (b) temperature range for the phase transition from orthorhombic to tetragonal of $MA_xFA_{1-x}PbI_3$ (x = 0.8, 0.6, 0.4 and 0.2), (c) PL peak energy range for the phase transition from orthorhombic to tetragonal of $MA_xFA_{1-x}PbI_3$ (x = 0.8, 0.6, 0.4 and 0.2), and (d) $\Delta E/\Delta T$ of $MA_xFA_{1-x}PbI_3$ (x = 0.8, 0.6, 0.4 and 0.2).

this temperature range is a mixed and unstable state, which is very sensitive to heat. Phase transition ranges are very different as the proportion of MA in $MA_xFA_{1-x}PbI_3$ changes. As shown in Fig. S3,† $MA_{0.6}FA_{0.4}PbI_3$ and $MA_{0.4}FA_{0.6}PbI_3$ show gentler phase transition than others. Phase transition ranges of the four samples, $MA_xFA_{1-x}PbI_3$ (x = 0.8, 0.6, 0.4 and 0.2), are denoted in Fig. 5b. Red circles mark the end temperature of phase transition, and the blue circles mark the start temperature of the phase transition. Phase transition ranges of $MA_{0.6}FA_{0.4}PbI_3$ and $MA_{0.4}FA_{0.6}PbI_3$ are significantly larger than that of $MA_{0.8}FA_{0.2}PbI_3$ and $MA_{0.2}FA_{0.8}PbI_3$, as shown in Fig. 5b. The inset of Fig. 5b shows the temperature changes in the phase transition ranges (ΔT) of four samples. Note that there is no start point for the pure $MAPbI_3$, as can be seen in Fig. 4a. This is because the complete phase transition of $MAPbI_3$ takes place at temperatures lower than 30 K.

The PL peak energy shifts in the phase transition ranges were also explored, as shown in Fig. 5c, and the inset shows the energy shift (ΔE) of the four samples. Both ΔT and ΔE are wider, whereas the proportions of MA and FA are similar. To analyze the temperature-related stability, $\Delta E/\Delta T$, indicating an average energy shift per Kelvin, has been calculated and plotted in Fig. 5d. $\Delta E/\Delta T$ reaches its minimum at x = 0.4, indicating that the perovskite material of this constituent is more stable. The phase transition process for this sample would be gentle as the temperature changes. While the proportions of MA or FA are comparable in the crystal structure, $\Delta E/\Delta T$ would be larger. This means the PL peak energy shifts at a faster rate as the temperature changes and so does the bandgap. In this regard, the value of $\Delta E/\Delta T$ shows stability of the structure of perovskite materials. As is known, the changes of bandgaps result from the changes of Pb–I–Pb angles, and this has been

widely investigated.[25] The faster changing rate of bandgaps means the faster changing rate of Pb–I–Pb angles, in other words, structures. For the mixed organic cation perovskite materials, strains would be important for the formation of the final structure as the Pb–I–Pb angles change. If the proportions of MA and FA are comparable, strains induced by $MAPbI_3$ and $FAPbI_3$ just compromise with each other as they have different phase behaviours caused by the rotation of cations.[34] Since strains distribute uniformly as the cations distribute in a random manner, which has been abovementioned already, the structure, therefore, is stable when the temperature changes. As the proportion of either of the two cations increases to a dominant position, strains induced at the boundaries of two different molecules become less. In addition, the whole lattice structure behaves like the pure cation perovskite, which much easily displays a phase transition and possesses poor stability.

4. Conclusions

In conclusion, we have investigated the structural properties of mixed organic cation perovskites $MA_xFA_{1-x}PbI_3$ (x = 1, 0.8, 0.6, 0.4 and 0.2). At first, structures composed of uniformly distributed FA and MA molecules have been comparatively discussed. It is found that all these samples display cubic phases at room temperature, and the lattice size becomes larger as the proportion of FA increases. Comprehensive temperature- and power-dependent PL measurements have been carried out to study the phase transitions and optical properties induced by different crystal structures. Pure $MAPbI_3$ demonstrates multi-peak emission at low temperatures (30 K), which shows quite different emission properties. Limited amount of orthorhombic phase in $MAPbI_3$ was observed, resulting in a clear energy transfer in the crystal under high power excitation. In addition, it further confirms the co-existence of orthorhombic and tetragonal phases and is instructive in terms of the synthesis of perovskites. Optical properties are similar for mixed organic cation perovskites at both room and low temperatures. Formation of free excitons assisted by thermally activated carriers contributes to photoemission in mixed-type perovskites, whereas this process is not observed in pure $MAPbI_3$. However, the recombination of free excitons is depressed by exciton–exciton interaction for all these samples under high excitation power at room temperature. Variations in the PL peak positions resulting from the change in temperature shed light on the analysis of stability for mixed organic cation perovskites. If the proportions of FA and MA are comparable, the phase transition process of the sample would be gentler as compared to that of the single-species cation-dominant structure. The structural stability against temperature is attributed to uniformly distributed strains existing at the boundaries of $MAPbI_3$ and $FAPbI_3$ molecules in mixed organic cation perovskites. The analysis of this structural stability would be meaningful for the future practical use of mixed organic cation perovskites.

Conflicts of interest

There are no conflicts to declare.

Acknowledgements

This work was supported by the National Natural Science Foundation of China (11574130 and 61775091), the Shenzhen Science and Technology Innovation Commission (Projects No. KQJSCX20170726145748464, JCYJ20150529152146471, and KQTD2015071710313656), and the Shenzhen Key Laboratory Project (No. ZDSYS201602261933302).

Notes and references

1 J. H. Noh, S. H. Im, J. H. Heo, T. N. Mandal and S. I. Seok, *Nano Lett.*, 2013, **13**, 1764–1769.
2 G. E. Eperon, S. D. Stranks, C. Menelaou, M. B. Johnston, L. M. Herz and H. J. Snaith, *Energy Environ. Sci.*, 2014, **7**, 982–988.
3 C. Wehrenfennig, M. Liu, H. J. Snaith, M. B. Johnston and L. M. Herz, *J. Phys. Chem. Lett.*, 2014, **5**, 1300–1306.
4 S. D. Stranks, G. E. Eperon, G. Grancini, C. Menelaou, M. J. Alcocer, T. Leijtens, L. M. Herz, A. Petrozza and H. J. Snaith, *Science*, 2013, **342**, 341–344.
5 G. Xing, N. Mathews, S. Sun, S. S. Lim, Y. M. Lam, M. Grätzel, S. Mhaisalkar and T. C. Sum, *Science*, 2013, **342**, 344–347.
6 G. Xing, N. Mathews, S. S. Lim, N. Yantara, X. Liu, D. Sabba, M. Gratzel, S. Mhaisalkar and T. C. Sum, *Nat. Mater.*, 2014, **13**, 476–480.
7 D. P. McMeekin, G. Sadoughi, W. Rehman, G. E. Eperon, M. Saliba, M. T. Hörantner, A. Haghighirad, N. Sakai, L. Korte and B. Rech, *Science*, 2016, **351**, 151–155.
8 K. T. Cho, S. Paek, G. Grancini, C. Roldán-Carmona, P. Gao, Y. Lee and M. K. Nazeeruddin, *Energy Environ. Sci.*, 2017, **10**, 621–627.
9 W. S. Yang, B.-W. Park, E. H. Jung, N. J. Jeon, Y. C. Kim, D. U. Lee, S. S. Shin, J. Seo, E. K. Kim and J. H. Noh, *Science*, 2017, **356**, 1376–1379.
10 Y. Cao, N. Wang, H. Tian, J. Guo, Y. Wei, H. Chen, Y. Miao, W. Zou, K. Pan, Y. He, H. Cao, Y. Ke, M. Xu, Y. Wang, M. Yang, K. Du, Z. Fu, D. Kong, D. Dai, Y. Jin, G. Li, H. Li, Q. Peng, J. Wang and W. Huang, *Nature*, 2018, **562**, 249–253.
11 K. Lin, J. Xing, L. N. Quan, F. P. G. de Arquer, X. Gong, J. Lu, L. Xie, W. Zhao, D. Zhang, C. Yan, W. Li, X. Liu, Y. Lu, J. Kirman, E. H. Sargent, Q. Xiong and Z. Wei, *Nature*, 2018, **562**, 245–248.
12 T. S. Kao, Y. H. Chou, K. B. Hong, J. F. Huang, C. H. Chou, H. C. Kuo, F. C. Chen and T. C. Lu, *Nanoscale*, 2016, **8**, 18483–18488.

This journal is © The Royal Society of Chemistry 2019

13 G. L. Whitworth, J. R. Harwell, D. N. Miller, G. J. Hedley, W. Zhang, H. J. Snaith, G. A. Turnbull and I. D. Samuel, *Opt. Express*, 2016, **24**, 23677–23684.
14 J. H. Heo, S. H. Im, J. H. Noh, T. N. Mandal, C.-S. Lim, J. A. Chang, Y. H. Lee, H.-j. Kim, A. Sarkar, M. K. Nazeeruddin, M. Grätzel and S. I. Seok, *Nat. Photonics*, 2013, **7**, 486–491.
15 N. J. Jeon, J. H. Noh, Y. C. Kim, W. S. Yang, S. Ryu and S. I. Seok, *Nat. Mater.*, 2014, **13**, 897–903.
16 Y.-Y. Zhang, S. Chen, P. Xu, H. Xiang, X.-G. Gong, A. Walsh and S.-H. Wei, *Chin. Phys. Lett.*, 2018, **35**, 036104.
17 G. Nagabhushana, R. Shivaramaiah and A. Navrotsky, *Proc. Natl. Acad. Sci. U. S. A.*, 2016, **113**, 7717–7721.
18 O. J. Weber, B. Charles and M. T. Weller, *J. Mater. Chem. A*, 2016, **4**, 15375–15382.
19 A. Binek, F. C. Hanusch, P. Docampo and T. Bein, *J. Phys. Chem. Lett.*, 2015, **6**, 1249–1253.
20 X. Zhang, H. Liu, W. Wang, J. Zhang, B. Xu, K. L. Karen, Y. Zheng, S. Liu, S. Chen, K. Wang and X. W. Sun, *Adv. Mater.*, 2017, **29**, 1606405.
21 N. Pellet, P. Gao, G. Gregori, T. Y. Yang, M. K. Nazeeruddin, J. Maier and M. Gratzel, *Angew. Chem., Int. Ed.*, 2014, **53**, 3151–3157.
22 W. S. Yang, J. H. Noh, N. J. Jeon, Y. C. Kim, S. Ryu, J. Seo and S. I. Seok, *Science*, 2015, **348**, 1234–1237.
23 T. Oku, in *Solar Cells - New Approaches and Reviews*, 2015, ch. 3, DOI: 10.5772/59284.
24 N. J. Jeon, J. H. Noh, W. S. Yang, Y. C. Kim, S. Ryu, J. Seo and S. I. Seok, *Nature*, 2015, **517**, 476–480.
25 M. R. Filip, G. E. Eperon, H. J. Snaith and F. Giustino, *Nat. Commun.*, 2014, **5**, 5757.
26 Y. Yamada, T. Nakamura, M. Endo, A. Wakamiya and Y. Kanemitsu, *J. Am. Chem. Soc.*, 2014, **136**, 11610–11613.
27 J. Even, L. Pedesseau and C. Katan, *J. Phys. Chem. C*, 2014, **118**, 11566–11572.
28 M. I. Dar, G. Jacopin, S. Meloni, A. Mattoni, N. Arora, A. Boziki, S. M. Zakeeruddin, U. Rothlisberger and M. Grätzel, *Sci. Adv.*, 2016, **2**, e1601156.
29 S. A. Shojaee, T. A. Harriman, G. S. Han, J. K. Lee and D. A. Lucca, *Appl. Phys. Lett.*, 2017, **111**, 023902.
30 H.-H. Fang, R. Raissa, M. Abdu-Aguye, S. Adjokatse, G. R. Blake, J. Even and M. A. Loi, *Adv. Funct. Mater.*, 2015, **25**, 2378–2385.
31 B. T. Diroll, P. Guo and R. D. Schaller, *Nano Lett.*, 2018, **18**, 846–852.
32 W. Kong, Z. Ye, Z. Qi, B. Zhang, M. Wang, A. Rahimi-Iman and H. Wu, *Phys. Chem. Chem. Phys.*, 2015, **17**, 16405–16411.
33 H. H. Fang, L. Protesescu, D. M. Balazs, S. Adjokatse, M. V. Kovalenko and M. A. Loi, *Small*, 2017, **13**, 1700673.
34 M. T. Weller, O. J. Weber, P. F. Henry, A. M. Di Pumpo and T. C. Hansen, *Chem. Commun.*, 2015, **51**, 4180–4183.

This journal is © The Royal Society of Chemistry 2019